



Tribo–Mechanical Properties of HVOF-Sprayed NiMoAl-Cr₂AlC Composite Coatings

Deepak Davis¹ · Sheela Singh² · R. P. S. Chakradhar³ · Meenu Srivastava³

Submitted: 26 October 2019 / in revised form: 2 July 2020 / Published online: 21 July 2020
© ASM International 2020

Abstract The tribo-mechanical properties of NiMoAl-Cr₂AlC MAX phase composite coatings on stainless steel substrate have been investigated. NiMoAl with different amounts of Cr₂AlC (10, 20, 50 and 100 wt.%) were prepared by turbo-mixing and deposited by High-Velocity Oxy-Fuel (HVOF) method on stainless steel substrate. The phase composition, microstructure, chemical composition, tribological and mechanical properties of the coatings were analyzed using x-Ray Diffraction (XRD), Field Emission Scanning Electron Microscope (FESEM), Energy-Dispersive x-ray analysis (EDAX), pin-on-disk wear testing rig and nanohardness tester, respectively. The worn surfaces were analyzed by metallurgical optical microscope, FESEM and three-dimensional surface profiler to understand the wear behavior in detail. The addition of the Cr₂AlC MAX phase in NiMoAl enhances the mechanical properties and reduces the surface roughness and porosity. NiMoAl-20 wt.% Cr₂AlC and Cr₂AlC coatings containing equal amounts of oxygen and carbon in the tribofilm show

the low coefficient of friction (COF) and wear rate. The addition of the Cr₂AlC MAX phase in the NiMoAl matrix up to 20 wt.% reduces the wear rate by one order of magnitude and enhances the coating life by 7000 twist fatigue cycles.

Keywords Cr₂AlC MAX phase · HVOF coating · NiMoAl alloy · tribology · twist fatigue

Introduction

In the automotive sector, the engine components usually undergo frictional losses due to the sliding contact of the piston ring and the cylinder liner which accounts for 20% of overall energy loss in the engine (Ref 1). Gray cast iron is a well-known material for the piston ring application because of its oil-retaining capacity, thereby providing lubrication even under starved condition. The severity of wear surface damage, adhesion and material cracking are the main problem of gray cast iron-based piston rings (Ref 2). To lessen these tribological issues, martensitic stainless steel was introduced (Ref 3). Martensitic stainless steel piston rings show better corrosion resistance, good physical and mechanical properties, but low scuffing resistance (Ref 4). To overcome the scuffing problems, Ni-Mo-based coatings were introduced. The performance of Ni-Mo alloy can be further improved by the addition of aluminum (Al). Additions of Al can protect the Ni-Mo alloy by formation of a tightly adherent alumina scale at high temperature that resists attack by oxidation, carburization and chlorination (Ref 5-7). Molybdenum and nickel coatings provide self-lubrication under dry conditions, better scuffing resistance and improve the thermal conductivity (Ref 8). However, Ni-Mo coatings suffer high wear during the run-in periods

✉ Sheela Singh
sheela.s@srmmap.edu.in; sheela2k5@gmail.com

✉ Meenu Srivastava
meenusri@nal.res.in

¹ Advanced Materials Research Laboratory, Department of Nanotechnology, Faculty of Engineering and Technology, SRM Institute of Science and Technology (Deemed to be University), Chennai, Tamil Nadu 603203, India

² Department of Mechanical Engineering, School of Engineering and Applied Sciences, SRM University – AP, Andhra Pradesh, Neerukonda, Mangalagiri Mandal, Guntur, Andhra Pradesh 522502, India

³ Surface Engineering Division, Council of Scientific and Industrial Research - National Aerospace Laboratories, HAL Airport Road, Bengaluru, Karnataka 560 017, India

in the temperature range of 400 to 600 °C (Ref 8). To reduce the high run-in wear, solid lubricants like graphite, hexagonal boron nitride and molybdenum disulfide were added into the Ni-based matrix (Ref 9). The amount of solid lubricant in the matrix plays a significant function in the development of bulk self-lubricating materials combined with high mechanical strength (Ref 9). Sliney has reported that an addition of 10–20 wt.% of solid lubricant powder in the matrix improves the lubricating properties with no loss of strength (Ref 10).

Recent trend is focused on the development of MAX phase-based materials for high-temperature wear-resistant applications (Ref 11). A MAX phase compound has a general formula of $M_{n+1}AX_n$, where M indicates transition metal, A is a Group III or IV element and X is either C or N and n lies from 1 to 3 (Ref 11, 12). MAX phase compounds like Cr_2AlC , Ta_2AlC and their composites (Cr_2AlC/Ag , Ta_2AlC/Ag) show promising tribological properties up to 550 °C (Ref 11, 12). MAX phase compounds like Ta_2AlC , Ti_2AlC , Cr_2AlC and Ti_3SiC_2 tested against Ni-based superalloy disk at 550 °C, showing excellent tribological properties, which was attributed to their nano-laminated structure (Ref 11). Cr_2AlC MAX phase compound shows very good corrosion and oxidation resistance and mechanical properties. Its coefficient of thermal expansion (CTE) [$12 \times 10^{-6}/K$ (Ref 13)] is similar to the base material [martensitic stainless steel- $9.5\text{--}12 \times 10^{-6}/K$ (Ref 14)] and the coating powder [NiMoAl- $9.3\text{--}13 \times 10^{-6}/K$ (Ref 14)] which indicates that Cr_2AlC MAX phase could be an ideal reinforcement for NiMoAl alloy used for piston ring coating.

The authors in the earlier study investigated the effect of Cr_2AlC addition on the NiMoAl matrix by air plasma spraying (APS) (Ref 15). However, during the APS process in air, the Cr_2AlC MAX phase got oxidized and produced oxides (Al_2O_3 and Cr_2O_3) and carbides (Cr_7C_3 and Cr_3C_2). This could be due to the high gas temperature of the APS process (approximately up to 16000 °C) (Ref 16). The present study is focused on investigating the tribo-mechanical performance of NiMoAl- Cr_2AlC MAX phase composite coatings by HVOF spraying. Cr_2AlC MAX phase is a group of ceramic materials, which have properties of metals too. It also possesses a layered structure with c/a ratio of 4.48 (Ref 17), which is the highest among known solid lubricant materials like MoS_2 (3.91) (Ref 18), BN (2.65) (Ref 19) and graphite (2.39) (Ref 20). It indicates that Cr_2AlC reinforcement has the potential for improving the tribo-mechanical properties of the NiMoAl matrix and is worth investigating. HVOF spray technique involves very high kinetic energy and low temperatures compared to air plasma spraying techniques and thereby achieving an outstanding cohesive strength between the deposited powders (Ref 21–23). This method has

progressed as a consistent technique to apply dense, uniform, hard, tribologically advanced and well adherent coatings to a vast range of applications (Ref 21, 24). Tribofilm formation on the worn surface is a key factor to reduce friction and wear (Ref 25, 26). In the present study, NiMoAl alloy coating with different amounts of Cr_2AlC (10, 20, 50, and 100 wt.%) was deposited on stainless steel substrate by HVOF process. The coatings were investigated for phase formation, microstructure, mechanical properties, tribological behavior and coating life cycle through twist fatigue test.

Experimental

Nickel (Ni), molybdenum (Mo) and aluminum (Al) powders (spherical morphology) with 99.2% purity were obtained from powder alloy corporation (Loveland, USA) and mixed using turbo mixer (room temperature, spin speed: 50 rpm, MXM 2, Insmart, India make) for about 2 h. This mixed powder is henceforth designated as NiMoAl (54, 44 and 2 wt.%). The Cr_2AlC MAX phase powders were prepared in-house using the method reported earlier (Ref 27). The resultant product was crushed and sieved using -325 mesh, to achieve the fine Cr_2AlC MAX phase powder.

As-synthesized Cr_2AlC MAX phase (10, 20 and 50 wt.%) and prepared NiMoAl alloy powders were mixed by turbo mixture (room temperature, spin speed: 50 rpm) for about 2 h. The prepared powders were preheated at 110 °C for one hour, before feeding into the spray unit. The composition of the prepared powders for the development of coatings is listed in Table 1. The prepared powders were deposited on stainless steel (SS-304) substrate by HIPOJET-2700 M spray gun using LPG as fuel and nitrogen as a carrier gas. The substrates were sandblasted at a pressure of 0.196 MPa using sand having a grit size of 75 μm , and the average roughness of the sandblasted surface was about 1.10 μm . The stand-off distance during sandblasting was maintained at 125 ± 5 mm. The sandblasted specimen substrates were cleaned with ethanol before the coating. Table 2 shows the process parameters adopted for spraying and all the coatings were prepared using the same parameters for comparison. The particle size distributions of the feedstock powders were analyzed by particle size analyzer (MS3000, Malvern Instruments Ltd., UK).

The phase composition of the coatings was analyzed using an x-ray diffractometer (XRD, Bruker D8 using $Cu K_\alpha$ radiation of wavelength 1.54 Å , step size: 0.0220 ($2\theta^\circ$), scan step time: 97.92 s). Surface morphology and elemental composition of the coatings were analyzed by field emission scanning electron microscopy (FESEM, Carl Zeiss, Supra 40 VP) and energy-dispersive x-ray analysis

Table 1 Elemental analysis of prepared coating powders for HVOF spraying

Coating details	Ni, wt.%	Mo, wt.%	Cr, wt.%	Al, wt.%	C, wt.%
NiMoAl	54.00	44.00	...	2.00	...
NiMoAl-10 wt.% Cr ₂ AlC	48.30	39.30	5.43	5.54	1.43
NiMoAl-20 wt.% Cr ₂ AlC	43.20	35.20	11.20	7.50	2.90
NiMoAl-50 wt.% Cr ₂ AlC	27.00	22.00	27.96	15.99	7.05
Cr ₂ AlC	55.99	29.98	14.03

Table 2 Process parameters adopted for HVOF spraying

Parameter	Value
Oxygen pressure	8 kg cm ⁻²
LPG pressure	6 kg cm ⁻²
Nitrogen pressure	6 kg cm ⁻²
Air pressure	6 kg cm ⁻²
Spray distance	300 mm
LPG flow	60 LPM
Oxygen flow	250 LPM
Carrier gas flow	20 LPM
Air flow	700 LPM
Powder feed rate	25 g min ⁻¹
Torch cycle	25 pass
Gun speed	600 mm s ⁻¹

(EDAX, Bruker, QUANTAX – XFlash), respectively. Porosity was measured by Image J software using FESEM images (secondary electron (SE) images, 1000× magnification) and average values from three of these measurements are reported (Ref 28). The surface roughness of the coated specimens was measured using a surface profiler (three-dimensional surface profiler, 3D Nano Map, 500 LS). The nanohardness and the elastic modulus (Oliver and Pharr method) were determined using nanoindentation testing (CSM instrument, Indenter type: Berkovich, Indenter material: Diamond) by employing a load of 10 mN for holding time of 10 s. The nanoindentation testing was performed across the cross section of the coatings, and the averages of ten measurements are reported. The wear behavior was investigated using a pin-on-disk tester using wear & friction monitor (TR-20L-PH200 - DUCOM, India) according to the ASTM G99 standard. Hemispherical shaped stainless steel pins (diameter 12 mm) were sprayed with the same powders and used for wear testing without subjecting them to any grinding operation. The coated pins are tested against a hard counter material (EN31 hardened steel disk, hardness is more than 680 VHN). The test parameters adopted are load—2 kg, speed—300 rpm, time duration—60 min and track diameter—60 mm. All the wear tests were performed at room temperature with the relative humidity of 55–60% under dry sliding conditions, and an average of three measurements are reported. After wear testing, the worn surface and its disk counterpart were

analyzed by a metallurgical optical microscope (Leica DM2700 M) and three-dimensional optical surface profiler (KLA Tencor, MicroXAM-800), respectively, for morphological changes. Further, the worn surfaces were analyzed by FESEM (Back scatter detector—BSE) and energy-dispersive x-ray analysis to understand the in-depth wear mechanism.

The fatigue life cycle of the NiMoAl and NiMoAl-20 wt.% Cr₂AlC coatings was examined by twist fatigue test. For that, the powders were coated over a 2.47 mm width and 200 μm groove depth piston ring with the same parameters mentioned in Table 2. The test was conducted as per ASTM E1049 standard in a Universal Testing Machine (UTM, Biss India Pvt. Ltd.). During the twist fatigue test, the two ends of the coated piston ring were clamped into the fixed and movable jaws of the system. The testing parameters like frequency, stroke length and constant load cell (the constant load applied to pull one of the free gap ends of the piston ring with constant magnitude at a fixed frequency) were fixed throughout the experiments as 1 Hz, 77.60 mm and 30 MPa, respectively (Ref 15). The test was continued until the coatings started peeling off and the test was repeated for three times to validate the result.

Results and Discussion

Characterization of Feedstock Powders

Figure 1(a–e) compares the x-ray diffraction (XRD) patterns of the feedstock powders. Figure 1(a) shows the XRD peaks corresponding to the presence of Ni (JCPDS No. 70-1849) and Mo (JCPDS No. 42-1120) only. The XRD peaks corresponding to Al were not observed, and it could be due to the low weight fraction of aluminum (2 wt.%). Figure 1(b–d) shows the XRD peaks corresponding to Ni, Mo and Cr₂AlC (JCPDS No. 89-2275) in NiMoAl-10 wt.% Cr₂AlC, NiMoAl-20 wt.% Cr₂AlC and NiMoAl-50 wt.% Cr₂AlC composite powders. Figure 1(e) shows the XRD peaks of the as-synthesized pure Cr₂AlC MAX phase.

Figure 2(a–e) compares the morphology of the feedstock powders by FESEM. Figure 2(a) shows the spherical particles of NiMoAl powder mixture. The individual average

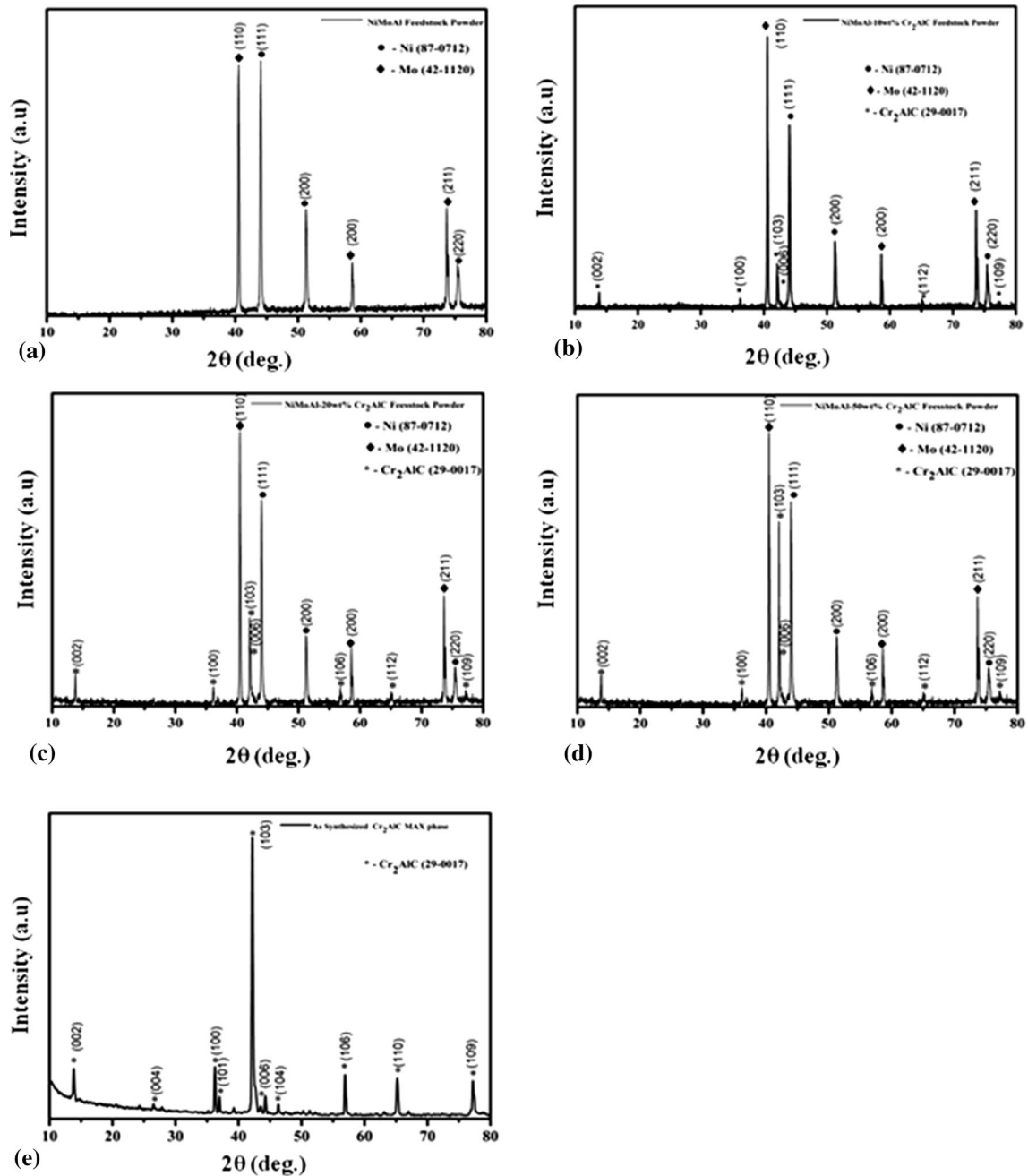
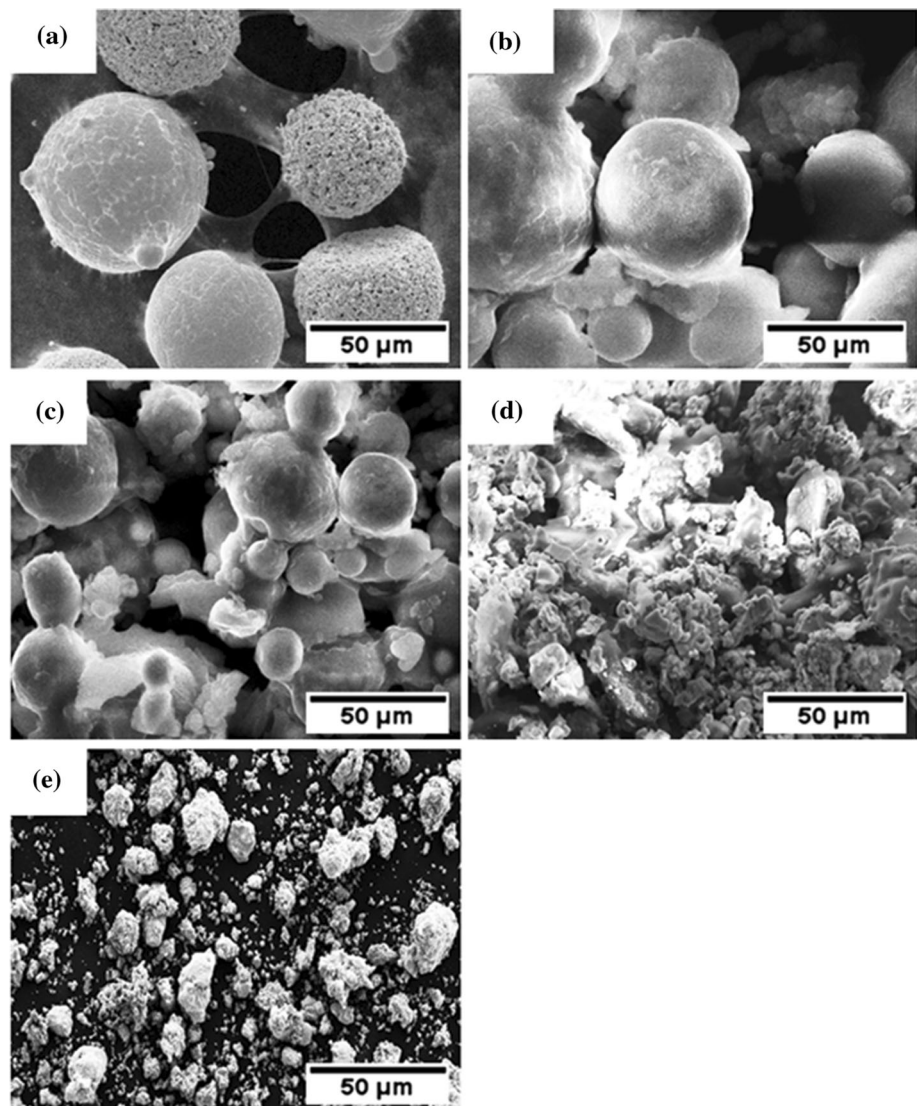


Fig. 1 XRD patterns of the feedstock powders, (a) NiMoAl, (b) NiMoAl-10 wt.% Cr₂AlC, (c) NiMoAl-20 wt.% Cr₂AlC, (d) NiMoAl-50 wt.% Cr₂AlC and (e) as-synthesized Cr₂AlC

size distributions of Ni, Mo and Al powder particles are observed to be $75 \pm 5 \mu\text{m}$, $68 \pm 5 \mu\text{m}$, and $65 \pm 10 \mu\text{m}$, respectively. Figure 2(b-d) shows the spherical particles of Ni and Mo with size in the range of 60 to $75 \mu\text{m}$ along with the aggregates of the Cr₂AlC MAX phase. The morphology in Fig. 2(d) shows a large amount of Cr₂AlC particles along with Mo and Ni which is confirmed through elemental mapping (Fig. 3). Figure 2(e) shows the aggregate of as-synthesized pure Cr₂AlC.

Figure 4(a-e) compares the particle size analysis of the feedstock powders. The average particle sizes are observed to be $70.98 \pm 1.50 \mu\text{m}$, $69.54 \pm 3.50 \mu\text{m}$, $68.12 \pm 4.00 \mu\text{m}$, $79.38 \pm 5.00 \mu\text{m}$ and $66.34 \pm 1.50 \mu\text{m}$, respectively, for the NiMoAl, NiMoAl-10 wt.% Cr₂AlC, NiMoAl-20 wt.% Cr₂AlC, NiMoAl-50 wt.% Cr₂AlC and Cr₂AlC feedstock powders.

Fig. 2 FESEM images of the feedstock powders, (a) NiMoAl, (b) NiMoAl-10 wt.% Cr₂AlC, (c) NiMoAl-20 wt.% Cr₂AlC, (d) NiMoAl-50 wt.% Cr₂AlC and (e) as-synthesized Cr₂AlC



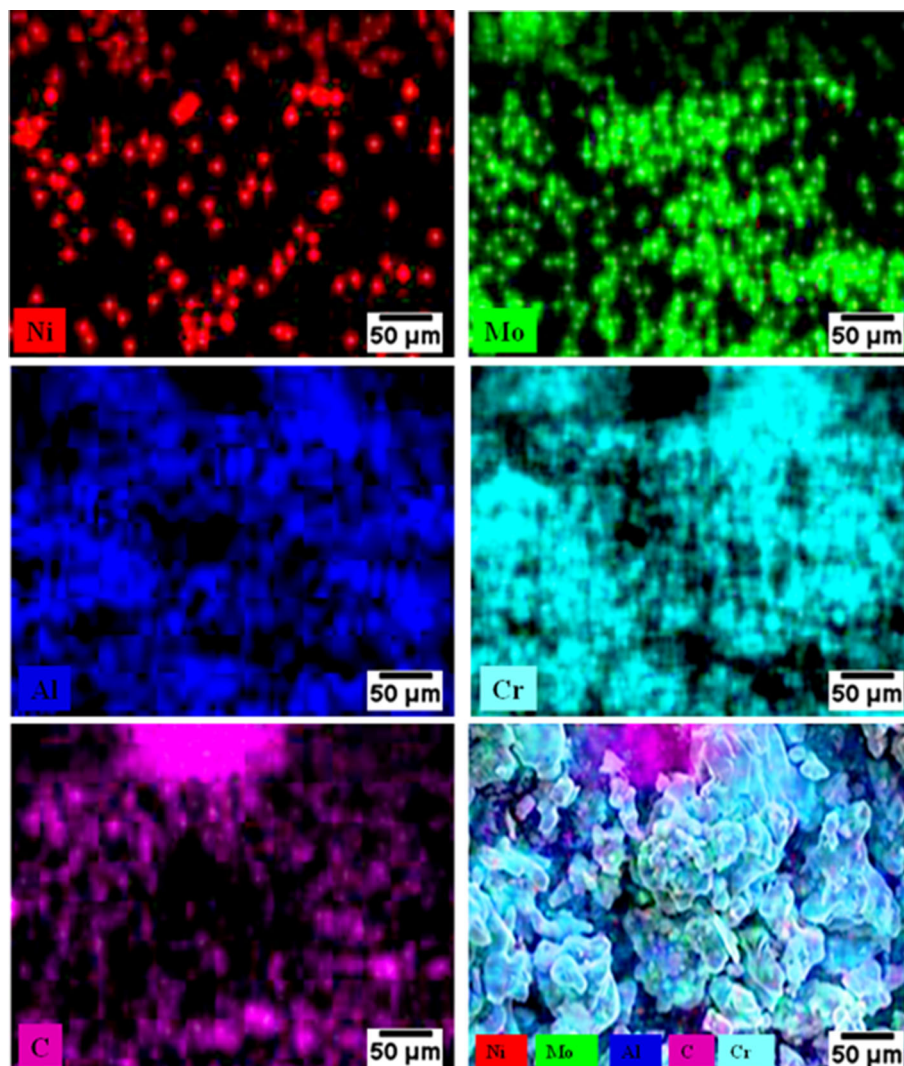
Characterization of Coatings

Phase Analysis

Figure 5(a-e) compares the x-ray diffraction patterns of HVOF-sprayed NiMoAl, NiMoAl-10 wt.% Cr₂AlC, NiMoAl-20 wt.% Cr₂AlC, NiMoAl-50 wt.% Cr₂AlC and Cr₂AlC specimens, respectively. The XRD peaks observed in Fig. 5(a) show the phases corresponding to Ni and Mo only. The distinct x-ray diffraction peaks at $2\theta = 40.23^\circ$, 58.59° , 73.65° and 87.63° correspond to the lattice planes of body-centered cubic (BCC) molybdenum (JCPDS No. 42-1120). The XRD peak at $2\theta = 44.54^\circ$ belongs to the (111) plane of face-centered cubic (FCC) nickel (JCPDS No. 70-1849). The XRD peak corresponding to Al was not observed, and it could be due to the low weight fraction of aluminum. Gao et al. (Ref 29) studied the solar absorbing properties of a Ni-Mo (Ni-70%, Mo-30%) coating obtained

by HVOF spraying and the coating showed the presence of Ni, Mo, NiO and MoNi₄ phases. However, in the present study, no oxide phase is observed, and this may be due to the reduced oxygen flow rate (250 LPM) and different feedstock powder composition. The formation of oxides depends on the fuel/oxygen ratio and in the present study the LPG/oxygen ratio was about 0.24 and at this particular ratio reduction in oxide phase formation is observed. However, as compared to the NiMoAl feedstock powder (Fig. 1a), the intensity of x-ray diffraction peaks corresponding to the Ni phase was reduced in its coating (Fig. 5a). This may be due to the evaporation of nickel at higher temperatures during the HVOF spraying and the lower deposition efficiency of Ni powders (Ref 30-32). Figure 5(b) shows the x-ray diffraction peaks corresponding to Mo and Ni. The absence of the Cr₂AlC phase was observed and it is associated with the lower weight fraction of the reinforcing phase. Figure 5(c) shows the x-ray diffraction peaks corresponding to Mo, Ni and

Fig. 3 Elemental mapping of NiMoAl-50 wt.% Cr₂AlC sample



Cr₂AlC. The peaks at $2\theta = 14.17^\circ$ and 42.18° are ascribed to the Cr₂AlC phase. The less intense XRD peaks of Cr₂AlC in NiMoAl-20 wt.% Cr₂AlC can be associated with the low scattering factor of Cr₂AlC. Figure 5(d) shows the x-ray diffraction peaks corresponding to Mo, Ni and Cr₂AlC. The intensity of the Cr₂AlC phase was increased as compared to NiMoAl-20 wt.% Cr₂AlC coating and it could be due to the higher weight fraction of the reinforcing phase. Figure 5(e) shows the XRD peaks at $2\theta = 14.17^\circ$, 36.23° , 36.95° , 42.19° , 42.38° , 51.26° , 56.81° , 63.09° , 76.99° , 77.15° and 80.81° which correspond to the hexagonal phase of Cr₂AlC (JCPDS No. 89-2275). Yang et. al. (Ref 33) reported the decomposition of the Cr₂AlC MAX phase into Cr₇C₃ during HVOF spraying.

In order to investigate the presence of minute phases, micro-Raman analysis (HORIBA France, LABRAM HR evolution, wavelength: 532 nm, magnification: 50×) was performed on the surface of the HVOF-coated Cr₂AlC

MAX phase sample. Figure 6 shows the presence of the pure Cr₂AlC phase corresponding to Raman shifts at 399.2 and 573.6 cm⁻¹ (Ref 17). The presence of any oxide phase was not observed. It indicates that the extent of Cr₂AlC oxidation during coating was minimal; hence, oxide phases were insignificant to be detected by Raman signal. This result is well in agreement with the x-ray diffraction pattern of the Cr₂AlC MAX phase coating (Fig. 5e). However, Raman peak shifts were observed in the Cr₂AlC coating as compared to as-synthesized Cr₂AlC powder. During the coating process, rapid cooling from a molten condition occurs which is expected to cause shifts in Raman spectra compared to those of the corresponding powders (Ref 34).

Morphology and Composition

Figure 7(a-e) displays the FESEM micrographs across the cross section of NiMoAl, NiMoAl-10 wt.% Cr₂AlC,

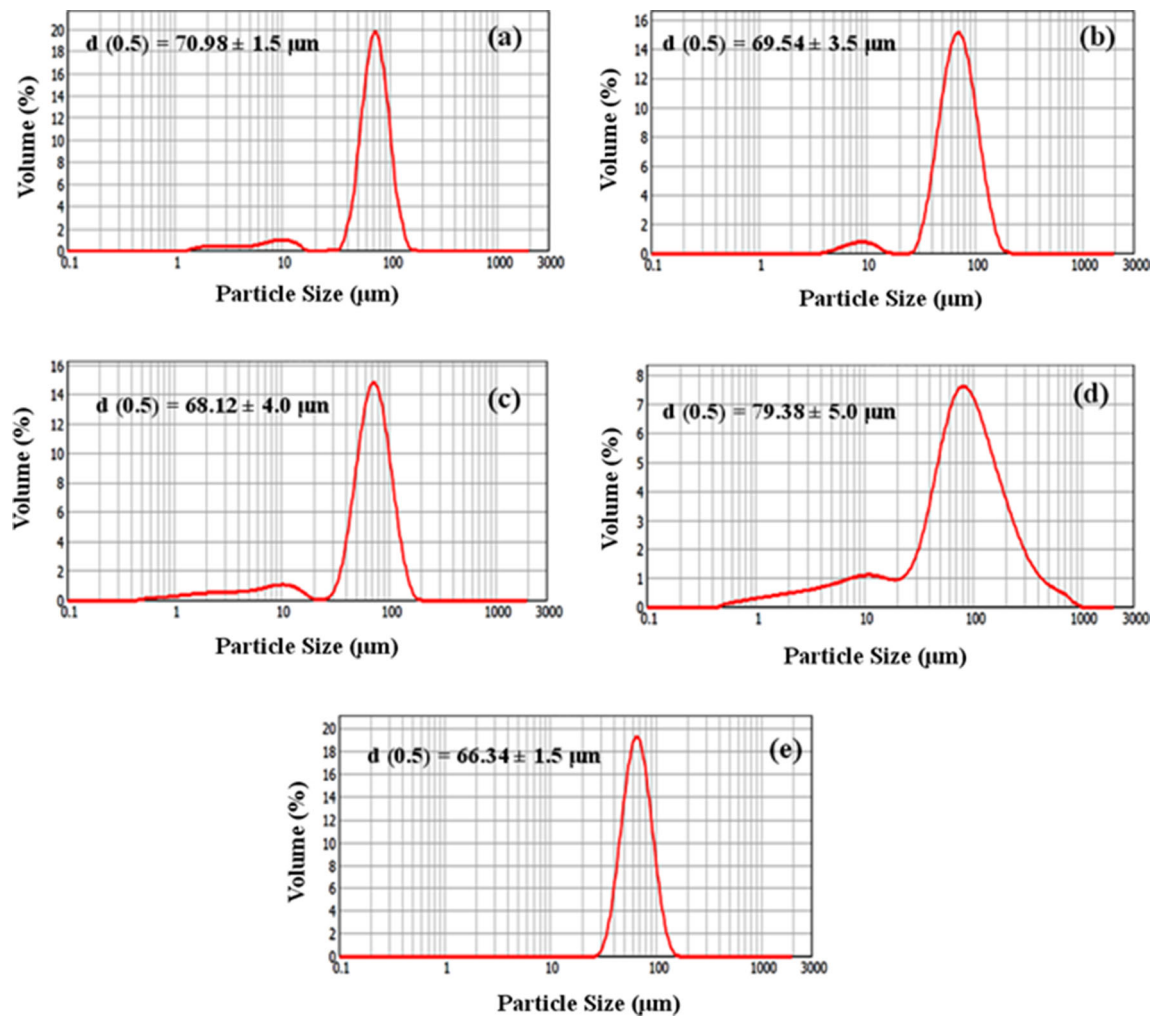


Fig. 4 Particle size analyzing of the feedstock powders (a) NiMoAl, (b) NiMoAl-10 wt.% Cr₂AlC, (c) NiMoAl-20 wt.% Cr₂AlC, (d) NiMoAl-50 wt.% Cr₂AlC and (e) Cr₂AlC

NiMoAl-20 wt.% Cr₂AlC, NiMoAl-50 wt.% Cr₂AlC and Cr₂AlC coatings, respectively. The average thickness of the coatings was determined using image analysis performed across the cross section of the coating. The thickness of NiMoAl, NiMoAl-10 wt.% Cr₂AlC, NiMoAl-20 wt.% Cr₂AlC, NiMoAl-50 wt.% Cr₂AlC and Cr₂AlC coatings are found to be $170 \pm 3 \mu\text{m}$, $105 \pm 5 \mu\text{m}$, $138 \pm 3 \mu\text{m}$, $135 \pm 5 \mu\text{m}$, and $141 \pm 8 \mu\text{m}$, respectively. All the coatings displayed a layered microstructure. The average porosity measurements of HVOF sprayed specimens obtained by Image J software are shown in Fig. 8(a-e). The average porosity of HVOF sprayed NiMoAl, NiMoAl-10 wt.% Cr₂AlC, NiMoAl-20 wt.% Cr₂AlC, NiMoAl-50 wt.% Cr₂AlC and Cr₂AlC coatings are found to be $4.63 \pm 2.50\%$, $3.60 \pm 3.00\%$, $2.13 \pm 1.25\%$, $1.95 \pm 1.55\%$ and $7.36 \pm 3.14\%$ respectively. The microstructure of NiMoAl alloy (Fig. 7a) shows a layered structure with distinct lamellae of Ni and Mo distributed

uniformly along relatively dense microstructure. A similar microstructure has been observed by Chen et al. in Ni-Mo-Al (Ni-5Mo-5Al wt.%) coating obtained by HVOF spraying (Ref 35, 36). In Fig. 7(b), the NiMoAl-10 wt.% Cr₂AlC coating shows a dense microstructure. However, as the reinforcing phase was increased to 20 wt.% (Fig. 7c), a further reduction in the volume of micropores was observed. The dense microstructure can be due to the addition of small size particles in a bigger size matrix thereby leading to the densification of the coating (Ref 16). The volume of the micropores in the NiMoAl-20 wt.% Cr₂AlC coating (Fig. 7c) is much smaller than it is in NiMoAl coating (Fig. 7a). Figure 7(d) shows the NiMoAl-50 wt.% Cr₂AlC coating with dense microstructure as compared to all other coatings along with the uniformly distributed Cr₂AlC phase. It could be due to the incorporation of the Cr₂AlC MAX phase and its size effect. The ceramic particles with fine size can significantly be

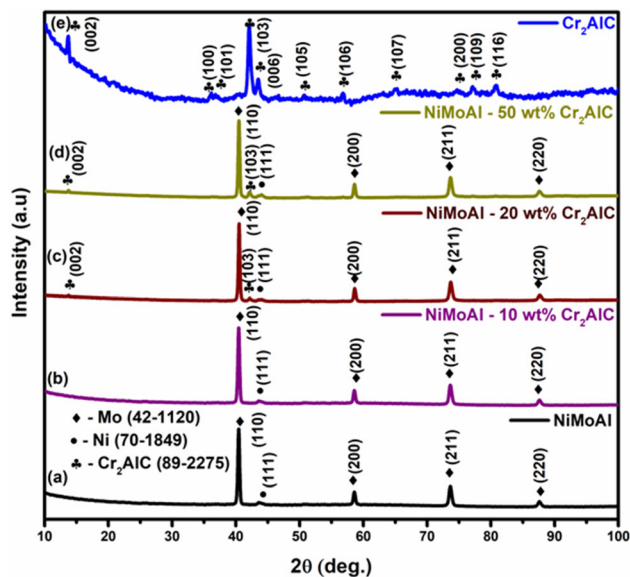


Fig. 5 X-ray diffraction patterns of HVOF-coated (a) NiMoAl, (b) NiMoAl-10 wt.% Cr₂AlC, (c) NiMoAl-20 wt.% Cr₂AlC, (d) NiMoAl-50 wt.% Cr₂AlC and (e) Cr₂AlC samples

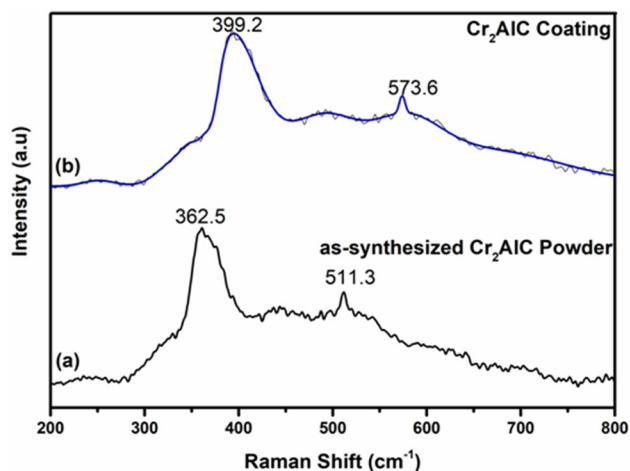


Fig. 6 Micro-Raman spectra of (a) as-synthesized Cr₂AlC MAX phase and (b) Cr₂AlC MAX phase coating

accumulated in the grain boundary and further lead to the densification of the matrix (Ref 37). As compared to NiMoAl and NiMoAl-20 wt.% Cr₂AlC coatings, the NiMoAl-50 wt.% Cr₂AlC coating exhibited predominantly interlamellar porosity (Fig. 8d), which was indicative of poor interfacial bonding. Figure 7(e) shows the lamellar deposition of Cr₂AlC with a large volume of interconnected pore and voids, which is confirmed through EDAX elemental mapping (Fig. 7f). Interlamellar pores with scattered orientation were prominent in the Cr₂AlC MAX phase coating (Fig. 8e). However, as compared with the NiMoAl matrix, the Cr₂AlC MAX phase possesses high melting point and this led to increases in the porosity of the pure MAX phase coating (Ref 38). Interlamellar pores with

scattered orientation were prominent in the Cr₂AlC MAX phase coating (Fig. 8e).

Figure 9(a-e) displays the surface morphology of HVOF sprayed NiMoAl, NiMoAl-10 wt.% Cr₂AlC, NiMoAl-20 wt.% Cr₂AlC, NiMoAl-50 wt.% Cr₂AlC and Cr₂AlC specimens obtained by using FESEM. Figure 9(a) shows the differences in size between rough Ni-based splats and smooth Mo-based splats. The dark-gray phase is rich in molybdenum and light gray is a nickel-rich phase, which is confirmed through elemental mapping (Fig. 9b). Gao et.al (Ref 29) and Chen et.al (Ref 35, 36) reported similar kind of surface morphology with micropores in HVOF-deposited Ni-Mo (70 Ni -30Mo wt.%) and Ni-Mo-Al (Ni-5Mo-5Al wt.%) alloys. Figure 9(c-f) displays the uniformly distributed rough splats of Ni, Mo and Cr₂AlC with dense microstructure. The Cr₂AlC MAX phase coating shows a granular structure with a grain size of less than 1 μm Fig. 9(f). The elemental compositions (EDAX) of the HVOF-coated specimens (on top surfaces) are illustrated in Table 3, and oxygen pickup in the range of 10-12 at.% is observed in the coatings. As compared with the elemental composition of the feedstock powders, the composition of the HVOF coated samples show a reduction in Ni content. This could be due to the evaporation of Ni and the differences in the deposition efficiencies of Ni and Mo (Ref 30-32).

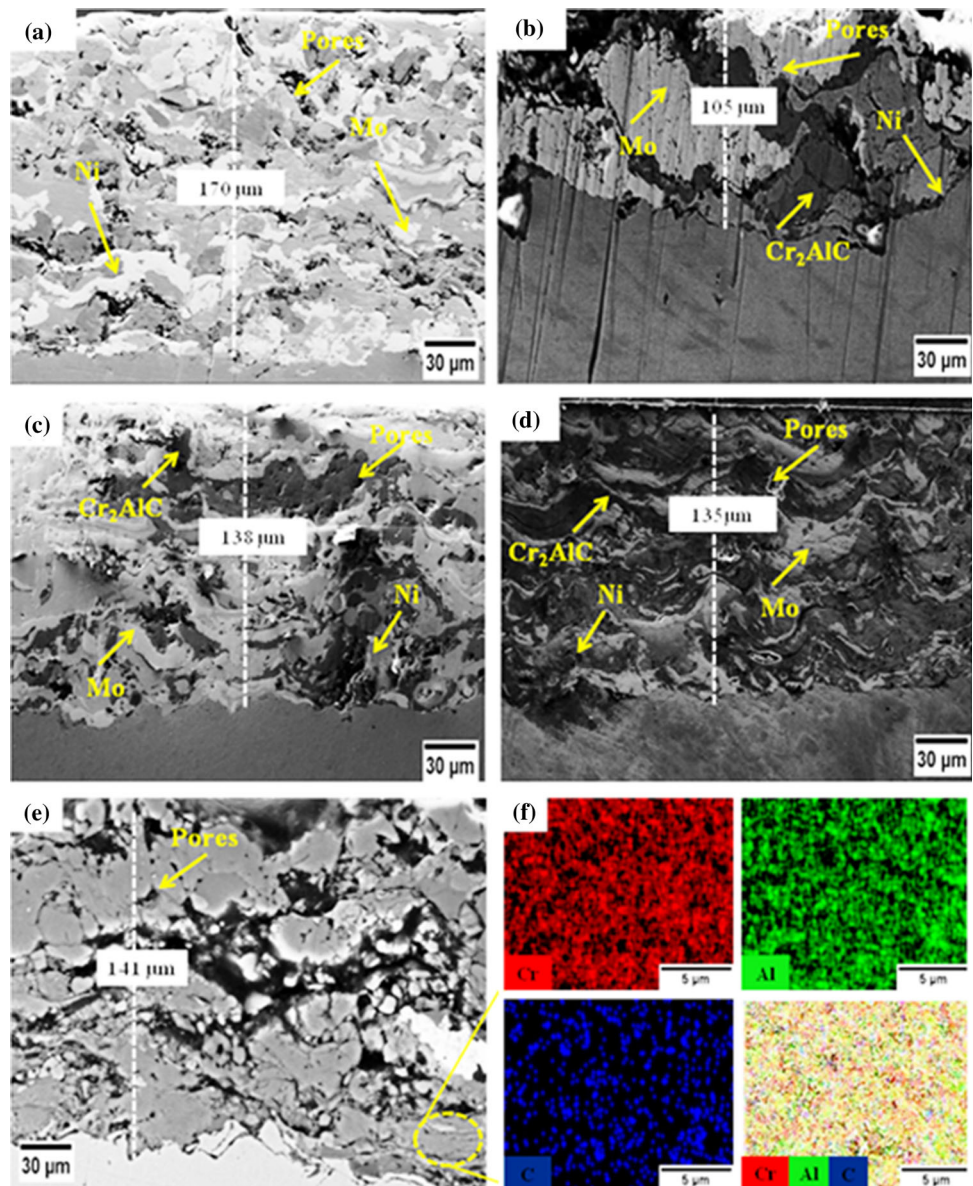
Mechanical Properties

The average nanohardness of the base material (SS), NiMoAl, NiMoAl-10 wt.% Cr₂AlC, NiMoAl-20 wt.% Cr₂AlC, NiMoAl-50 wt.% Cr₂AlC and Cr₂AlC coatings were found to be 250 ± 10, 390 ± 20, 446 ± 20, 501 ± 20, 637 ± 20 and 663 ± 20 VHN, respectively. The hardness value for NiMoAl coating is well in agreement with the reported values (410 ± 20 VHN) (Ref 35, 36). The nanohardness of NiMoAl coating significantly increased from 390 to 637 VHN with the addition of 50 wt.% Cr₂AlC MAX phase. The average elastic modulus of the base material (SS), NiMoAl, NiMoAl-10 wt.% Cr₂AlC, NiMoAl-20 wt.% Cr₂AlC, NiMoAl-50 wt.% Cr₂AlC and Cr₂AlC coatings are found to be 186 ± 2, 193 ± 4, 201 ± 5, 209 ± 3, 221 ± 6 and 264 ± 5 GPa, respectively. This shows that the incorporation of the Cr₂AlC MAX phase to the NiMoAl matrix led to an improvement in both hardness and elastic modulus. The reported bulk average elastic modulus of NiMo (Ref 39) and Cr₂AlC (Ref 40) are 183 ± 6 GPa and 282 ± 10 GPa, respectively, and it matches with the elastic modulus value of the coating developed in the present study.

Surface Roughness Analysis

Figure 10 shows the topographical profiles of (a) sand-blasted SS, (b) NiMoAl, (c) NiMoAl-10 wt.% Cr₂AlC,

Fig. 7 FESEM micrographs across the cross section of HVOF-coated (a) NiMoAl, (b) NiMoAl-10 wt.% Cr₂AlC, (c) NiMoAl-20 wt.% Cr₂AlC, (d) NiMoAl-50 wt.% Cr₂AlC, (e) Cr₂AlC and (f) elemental mapping of the Cr₂AlC MAX phase coating



(d) NiMoAl-20 wt.% Cr₂AlC, (e) NiMoAl-50 wt.% Cr₂AlC and (f) Cr₂AlC-coated samples. Uncoated sandblasted substrate showed a roughness of $1.1 \pm 0.5 \mu\text{m}$, whereas, NiMoAl, NiMoAl-10 wt.% Cr₂AlC, NiMoAl-20 wt.% Cr₂AlC, NiMoAl-50 wt.% Cr₂AlC and Cr₂AlC coatings showed an average roughness value of $7.2 \pm 0.3 \mu\text{m}$, $6.4 \pm 0.5 \mu\text{m}$, $5.0 \pm 0.4 \mu\text{m}$, $4.8 \pm 0.3 \mu\text{m}$ and $5.1 \pm 0.5 \mu\text{m}$, respectively. A significant reduction in the surface roughness value of NiMoAl coating is observed as compared to the reported value of $11.2 \mu\text{m}$ for NiMo (70 Ni-30 Mo wt.%) (Ref 29) and this could be due to the differences in operating condition and feedstock powder. The addition of fine Cr₂AlC MAX phase into the NiMoAl matrix led to a further reduction in surface roughness. The fine-sized ceramic particles during coating fill the gaps and

pores, which reduces the surface roughness of the coating (Ref 41).

Tribological Studies

The variation in the COF with respect to the time is shown in Fig. 11. The COF values obtained for the coatings against the hardened steel disk counterface are listed in Table 4. These results demonstrate that the tribological properties of NiMoAl coating are improved significantly with the additions of 10-20 wt.% Cr₂AlC MAX phase. However, in the NiMoAl-50 wt.% Cr₂AlC coating, the tribological properties had deteriorated. At higher volume fraction, the friction coefficient was found to be higher and there was no effect of reinforcement.

Fig. 8 Porosity measurements of HVOF coated (a) NiMoAl, (b) NiMoAl-10 wt.% Cr₂AlC, (c) NiMoAl-20 wt.% Cr₂AlC, (d) NiMoAl-50 wt.% Cr₂AlC and (e) Cr₂AlC samples

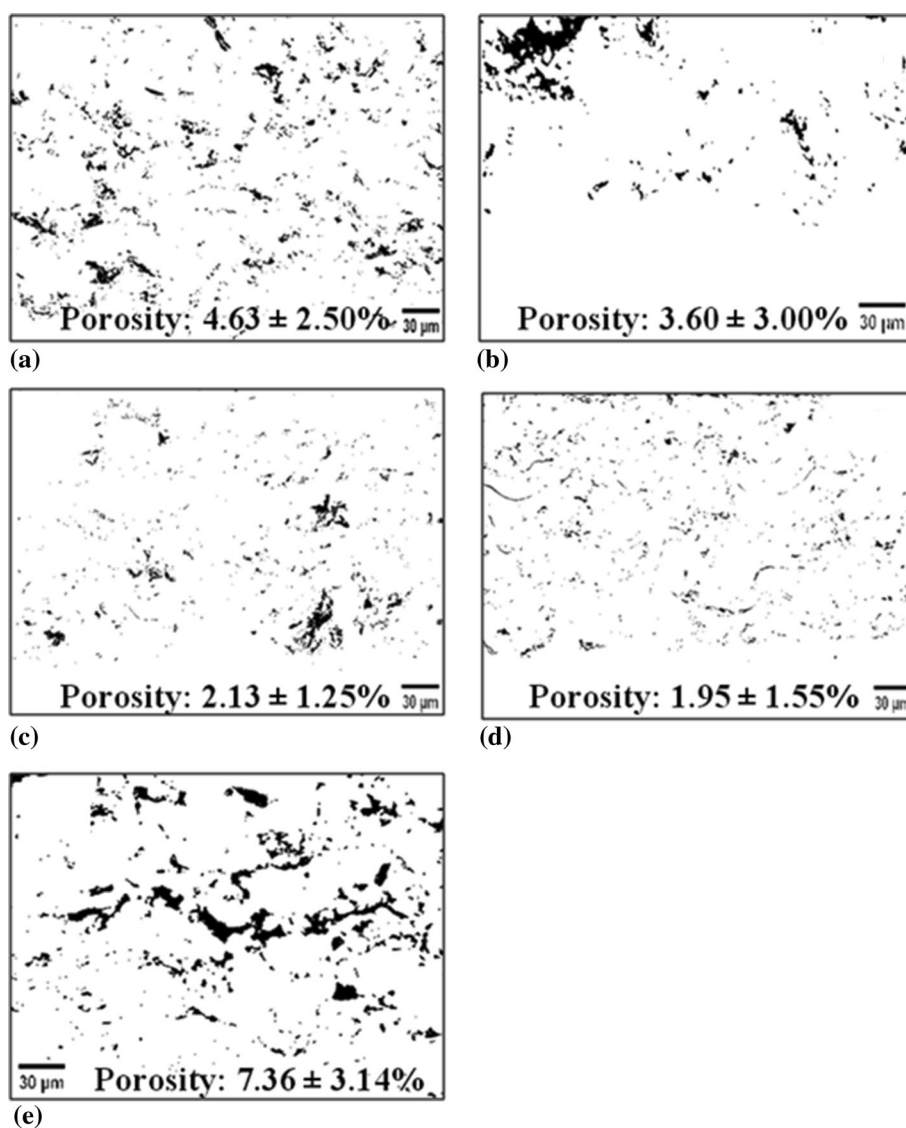
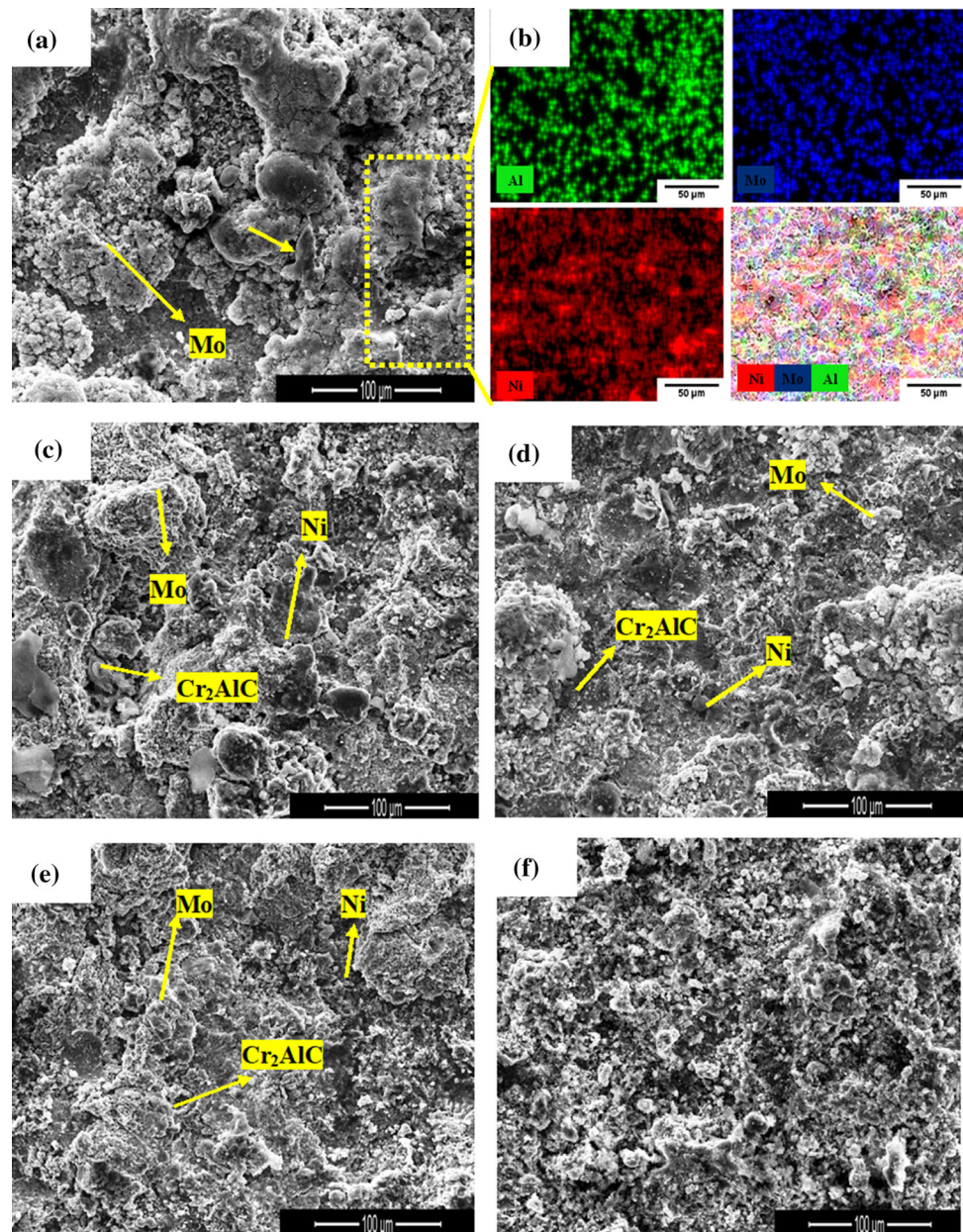


Figure 12 shows the worn surface of the coatings (a-e) and their corresponding disk counterparts (a'-e') imaged by an optical microscope. The worn surface of NiMoAl coating and the disk counterpart shows the formation of abrasive wear and adhesive wear (Fig. 12(a) and (a')). In Fig. 12(b), (c) and (e), iridescent layers were observed by optical microscopy and this is the sign of tribofilm formation (Ref 42). The transferred tribofilm has also been observed in the disk counterpart along with adhesive wear (Fig. 12(b'), (c') and (e')). Gupta et al. (Ref 43) also observed similar kinds of iridescent layers formed during the wear testing of the Cr₂AlC MAX phase against Inconel 718, Inconel 600 and alumina (pin-on-disk tribometer, sliding velocity: 1 m s⁻¹, load: 3 N). The local contact temperature during the tribo-test has resulted in the formation of tribofilm (Ref 44). They observed that the formation of tribofilm on the worn surface is the key factor for the reduction in the COF and wear rate. The wear scar area

is greater in the case of NiMoAl (Fig. 12a) and NiMoAl-50 wt.% Cr₂AlC coatings (Fig. 12d) as compared to other coatings as seen in Fig. 12.

Figure 13 shows the BSE micrograph of the worn surface of HVOF-coated NiMoAl, NiMoAl-10 wt.% Cr₂AlC, NiMoAl-20 wt.% Cr₂AlC, NiMoAl-50 wt.% Cr₂AlC and Cr₂AlC samples obtained by FESEM. Figure 13(a) shows the striped area of the NiMoAl coating with a set of similar scratches and this implies the formation of abrasive wear (Ref 41). The similar behavior is observed in Fig. 12(a). The hardness of the counter material (> 680 VHN) is more than that of the HVOF coated samples. Hence, abrasive wear was expected to be the key phenomenon (Ref 41). Figure 13(b-d) shows the worn surfaces of NiMoAl-10 wt.% Cr₂AlC, NiMoAl-20 wt.% Cr₂AlC, and NiMoAl-50 wt.% Cr₂AlC coatings with high fractions of plastically deformed area compared to NiMoAl coating with a smooth lubrication glaze (Ref 41). The development of smooth

Fig. 9 Surface morphology of HVOF coated samples by FESEM (a) NiMoAl, (b) elemental mapping of NiMoAl, (c) NiMoAl-10 wt.% Cr₂AlC, (d) NiMoAl-20 wt.% Cr₂AlC, (e) NiMoAl-50 wt.% Cr₂AlC and (f) Cr₂AlC



lubrication glaze (Fig. 13b-d) is due to the formation of oxide and carbide phases during the wear testing, which is confirmed through EDAX analysis. Figure 13(d) shows the abrasive wear on the surface NiMoAl-50 wt.% Cr₂AlC composite, and it could be due to a large amount of reinforcing phase in the matrix. The secondary phase (reinforcing phase) particles in the matrix play an important role in providing localized areas of high-stress concentrations that influenced the flow stress and the wear rate. The COF depends on the local contact pressure. The significance of this input depends on material nature and the volume of reinforcing the secondary phase (Ref 45). The incorporation of an excessively large amount of reinforcing phase

led to poor interfacial bonding to the matrix and increases the wear rate (Ref 46, 47). The worn surface of Cr₂AlC coating (Fig. 13e) shows adhesive wear with fine and brittle wear debris. In ceramics, plastic deformation on the wear surfaces is mainly due to the high compressive stress and the heat generated at the local contact area (Ref 48). Also, the wear debris with high flexibility can show higher plastic deformation during wear testing; hence, they may fill the open pores of the sample surface. This helps the coating surface to become smoother, thereby reducing the wear rate (Ref 49-51). The predicted wear mechanism is well in agreement with the FESEM (BSE) image of the worn surfaces (Fig. 13).

Table 3 EDAX analysis of HVOF-coated samples

Elements	NiMoAl coating		NiMoAl-10 wt.% Cr ₂ AiC coating		NiMoAl-20 wt.% Cr ₂ AiC coating		NiMoAl-50 wt.% Cr ₂ AiC coating		Cr ₂ AiC coating	
	at. %	wt. %	at. %	wt. %	at. %	wt. %	at. %	wt. %	at. %	wt. %
Mo	44.86 ± 2.0	64.79 ± 2.5	30.02 ± 2.80	48.61 ± 3.0	31.78 ± 2.30	49.88 ± 3.0	20.59 ± 2.80	38.74 ± 2.5		
Ni	28.10 ± 3.0	24.83 ± 4.0	34.08 ± 3.50	33.76 ± 4.0	27.49 ± 3.60	26.24 ± 4.5	15.85 ± 2.50	18.24 ± 3.0		
Cr	3.15 ± 0.90	2.47 ± 1.5	10.71 ± 3.40	9.40 ± 1.0	13.71 ± 1.00	11.60 ± 1.0	23.45 ± 1.60	23.91 ± 1.5	51.38 ± 1.3	72.81 ± 2.5
Al	4.16 ± 0.80	1.69 ± 0.8	3.60 ± 1.40	1.64 ± 0.5	4.11 ± 0.90	1.80 ± 0.5	13.12 ± 0.70	6.94 ± 0.8	24.25 ± 0.80	17.83 ± 2.0
O	10.27 ± 1.20	2.47 ± 0.5	8.13 ± 1.20	2.19 ± 0.8	9.2 ± 0.70	2.58 ± 0.8	12.15 ± 1.10	3.81 ± 0.5	12.64 ± 0.9	5.51 ± 0.5
Fe	2.30 ± 0.20	1.93 ± 0.5	1.80 ± 0.20	1.71 ± 0.5	5.98 ± 1.20	5.43 ± 0.5	4.45 ± 1.20	4.87 ± 0.3		
Si	2.20 ± 0.10	0.93 ± 0.8	1.23 ± 0.10	0.58 ± 0.5	5.16 ± 0.10	2.06 ± 0.5	3.25 ± 0.10	1.79 ± 0.3		
C	4.96 ± 0.09	0.89 ± 0.5	10.43 ± 1.10	2.11 ± 1.0	2.10 ± 0.80	0.41 ± 0.5	7.14 ± 0.80	1.70 ± 1.0	11.73 ± 1.23	3.85 ± 0.5
Total	100	100	100	100	100	100	100	100	100	100

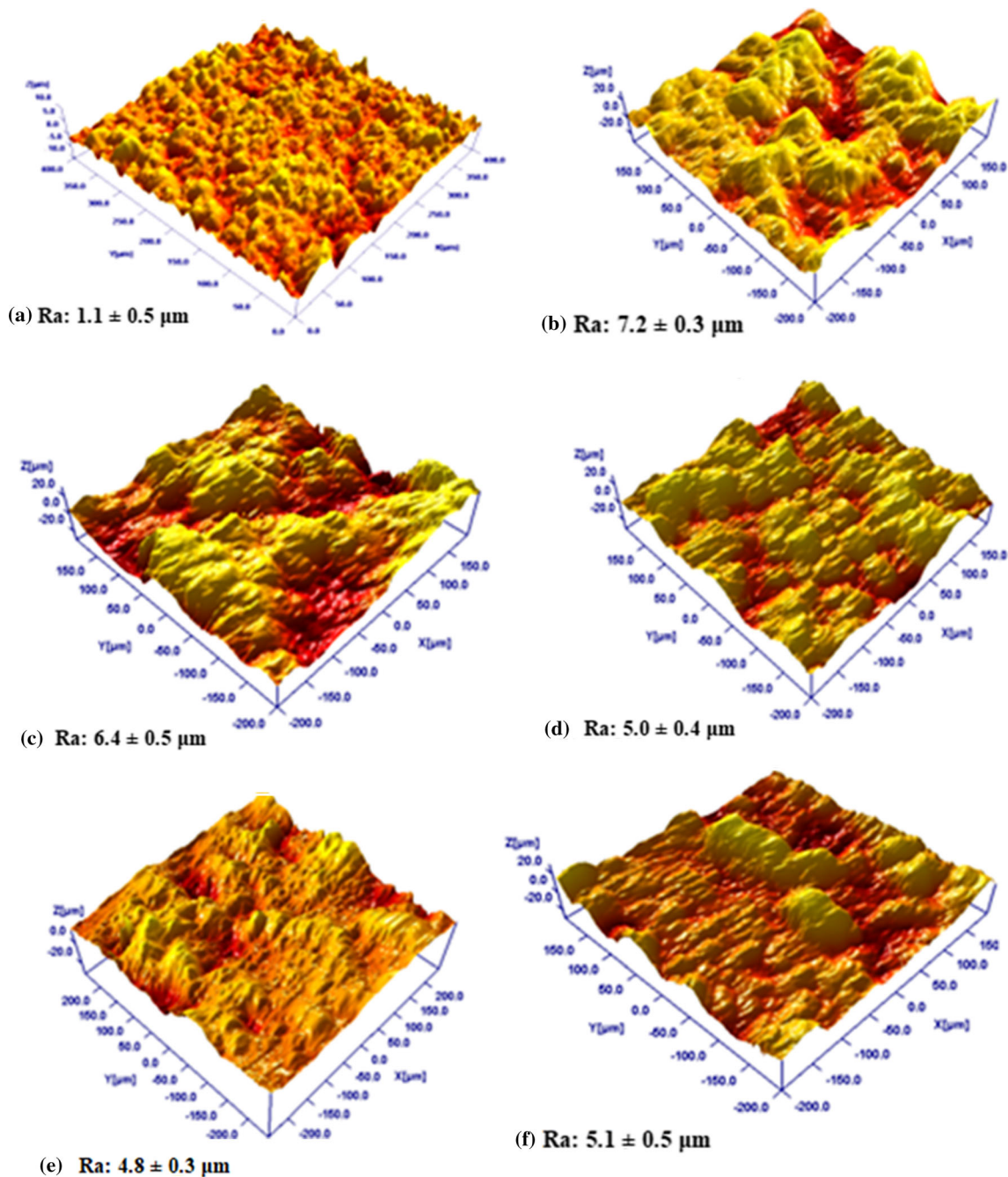


Fig. 10 Three-dimensional surface topography of different coatings on SS base material (a) uncoated sandblasted, (b) NiMoAl, (c) NiMoAl-10 wt.% Cr₂AlC, (d) NiMoAl-20 wt.% Cr₂AlC, (e) NiMoAl-50 wt.% Cr₂AlC and (f) Cr₂AlC samples

The average elemental compositions from EDAX analysis of the worn surfaces are shown in Fig. 14. The average composition of the worn surface of the HVOF-coated NiMoAl matrix is observed to be (Ni_{0.6} Mo_{0.26} Al_{0.01} Fe_{0.03} Cr_{0.03} C_{0.03} O_{0.07}). The presence of oxygen and carbon on the worn surface of NiMoAl coating (O:C = 2.3:1) could be due the tribochemical reaction between the contacting surfaces under high friction. The tribofilms formed on NiMoAl-10 wt.% Cr₂AlC ((Ni_{0.48} Mo_{0.13} Al_{0.03} Fe_{0.03}

Cr_{0.06} C_{0.07} O_{0.2}) and NiMoAl-50 wt.% Cr₂AlC ((Ni_{0.16} Mo_{0.13} Al_{0.07} Fe_{0.13} Cr_{0.08} C_{0.10} O_{0.33}) composites are enriched in carbon and oxygen as compared to NiMoAl coating (Fig. 14). The proportion of oxygen and carbon in the tribofilm of the NiMoAl-20 wt.% Cr₂AlC composite (Ni_{0.25} Mo_{0.23} Al_{0.04} Fe_{0.12} Cr_{0.07} C_{0.12} O_{0.17} and Cr₂AlC (Cr_{0.5} Al_{0.24} C_{0.10} Fe_{0.06}) O_{0.10} is 1.4:1 and 1:1, respectively. Among all compositions investigated, Cr₂AlC shows the lowest COF value (0.20 ± 0.05). It exhibits that

the tribofilm containing oxygen and carbon in an almost equal stoichiometry is lubricious and reduces the COF as observed in Cr₂AlC. NiMoAl-20 wt.% Cr₂AlC coating possessing O:C = 1.4:1 stoichiometry shows slightly higher COF than Cr₂AlC and less than that of NiMoAl-10 wt.% Cr₂AlC (O:C = 2.9:1) and NiMoAl-50 wt.% Cr₂AlC composites (O:C = 3.3:1) (Fig. 11 and 14). It shows that carbon and oxygen play an important role in the formation of friction film and it is related to the C-O adsorption layer (Ref 52, 53).

Figure 15 shows the surface topography image of the worn surface of HVOF-coated samples and their disk counterparts by the three-dimensional surface profiler. The worn surface of the NiMoAl coating and its disk counterpart (Fig. 15a) contain deep grooves in several areas. The worn surface of the HVOF-coated NiMoAl sample obtained by FESEM (Fig. 13a) is well in agreement with the surface topography image (Fig. 15a). As compared to the worn surface of the HVOF-coated NiMoAl coating and its disk counterpart, the NiMoAl-10 wt.% Cr₂AlC (Fig. 15b) shows a reduction in abrasive wear and it could be due to the addition of Cr₂AlC MAX phase in the NiMoAl matrix. The topography of the worn surface of the NiMoAl-20 wt.% Cr₂AlC coating and its disk counterpart show the thick tribofilm formation on the surfaces. The

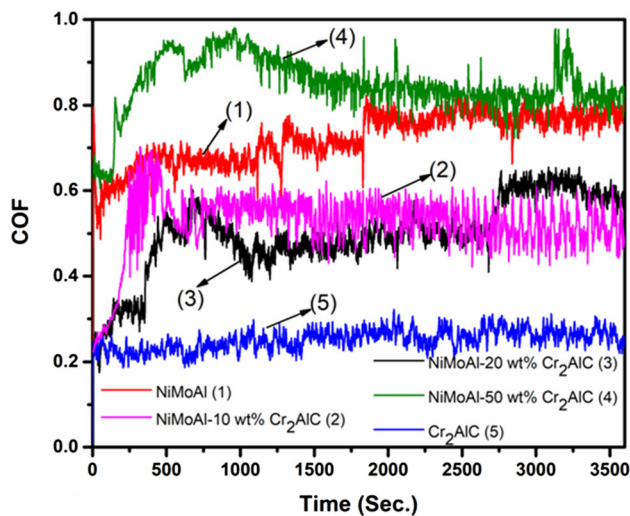


Fig. 11 COF with respect to the time graph of HVOF-coated samples

Table 4 COF and wear rate of the HVOF-coated samples

Coating details	Coefficient of friction (COF)	Wear rate, mm ³ N ⁻¹ m ⁻¹
NiMoAl	0.72 ± 0.04	1.05 × 10 ⁻⁵ (± 0.47)
NiMoAl-10 wt.% Cr ₂ AlC	0.52 ± 0.05	8.81 × 10 ⁻⁶ (± 0.32)
NiMoAl-20 wt.% Cr ₂ AlC	0.45 ± 0.03	4.98 × 10 ⁻⁶ (± 0.18)
NiMoAl-50 wt.% Cr ₂ AlC	0.83 ± 0.05	2.24 × 10 ⁻⁵ (± 0.29)
Cr ₂ AlC	0.20 ± 0.03	7.06 × 10 ⁻⁷ (± 0.53)

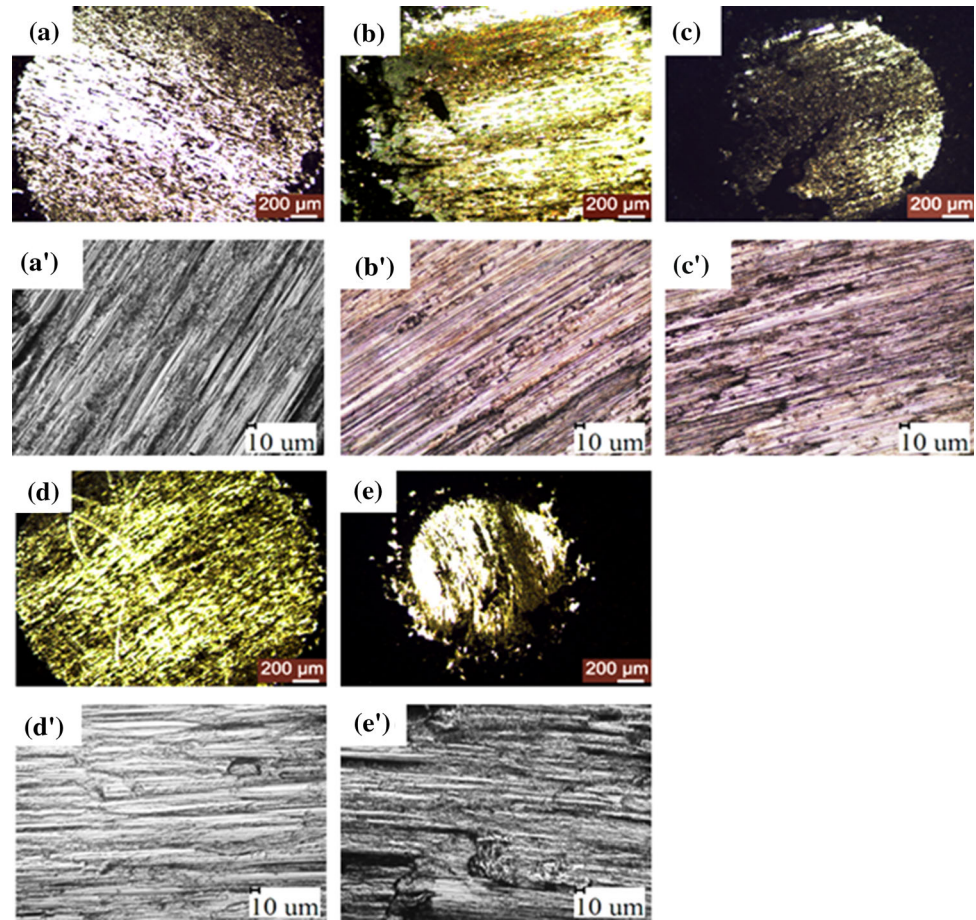
disk counterpart of the NiMoAl-20 wt.% Cr₂AlC coating shows a transferred tribofilm on the surface. This indicates the formation of homogeneous well adherent tribofilm on its surface during the wear test. However, the addition of 50 wt.% of Cr₂AlC in NiMoAl (Fig. 15d) led to increases in the formation of grooves on the worn surface and disk counterpart along with the abrasive wear. Figure 15(e) shows the worn surface of the Cr₂AlC coating and its disk counterpart. It shows thick tribofilm formation on the worn surface and transferred tribofilm on the disk counterpart. Thus, the reduced COF in the Cr₂AlC MAX phase coating was contributed by the surface smoothing due to the development of the homogenous tribofilm (Ref 54).

Based on the study, it can be concluded that up to 20 wt.% of Cr₂AlC MAX phase along with the tribofilm acts as a friction modifier in NiMoAl matrix. The Cr₂AlC MAX phase is a hexagonal-layered structure like h-BN and MoS₂ (Ref 11) and undergoes shearing in the direction of motion (Ref 55). Vazirisereshk et al. (Ref 56) and Scharf et al. (Ref 57) reported that the composite coating improves lubrication not only by the presence of the coating constituents but also by the lubricious products of chemical or physical reactions (tribofilm or transfer film) that happen during sliding. Among all NiMoAl-Cr₂AlC composites, the NiMoAl coating containing 20 wt.% Cr₂AlC displays the lowest COF and wear rate with optimum porosity (< 2.5%). The coating with a medium level of porosity is permissible for piston ring applications (Ref 8) because of its oil-retaining capacity which is mainly dependent on porosity. However, more porosity is observed in the pure Cr₂AlC MAX phase coating. The higher porosity level in the piston ring coating will reduce the strength of the piston rings (Ref 8). So based on the present study, NiMoAl containing 20 wt.% Cr₂AlC coating is recommended for piston ring applications.

Twist Fatigue Analysis

The wear rate of the NiMoAl coating is improved by one order of magnitude with the addition of 20 wt.% Cr₂AlC MAX phase, and it also shows the lowest COF. The porosity of NiMoAl-20 wt.% Cr₂AlC coating is comparable to that of NiMoAl-50 wt.% Cr₂AlC and is lower than

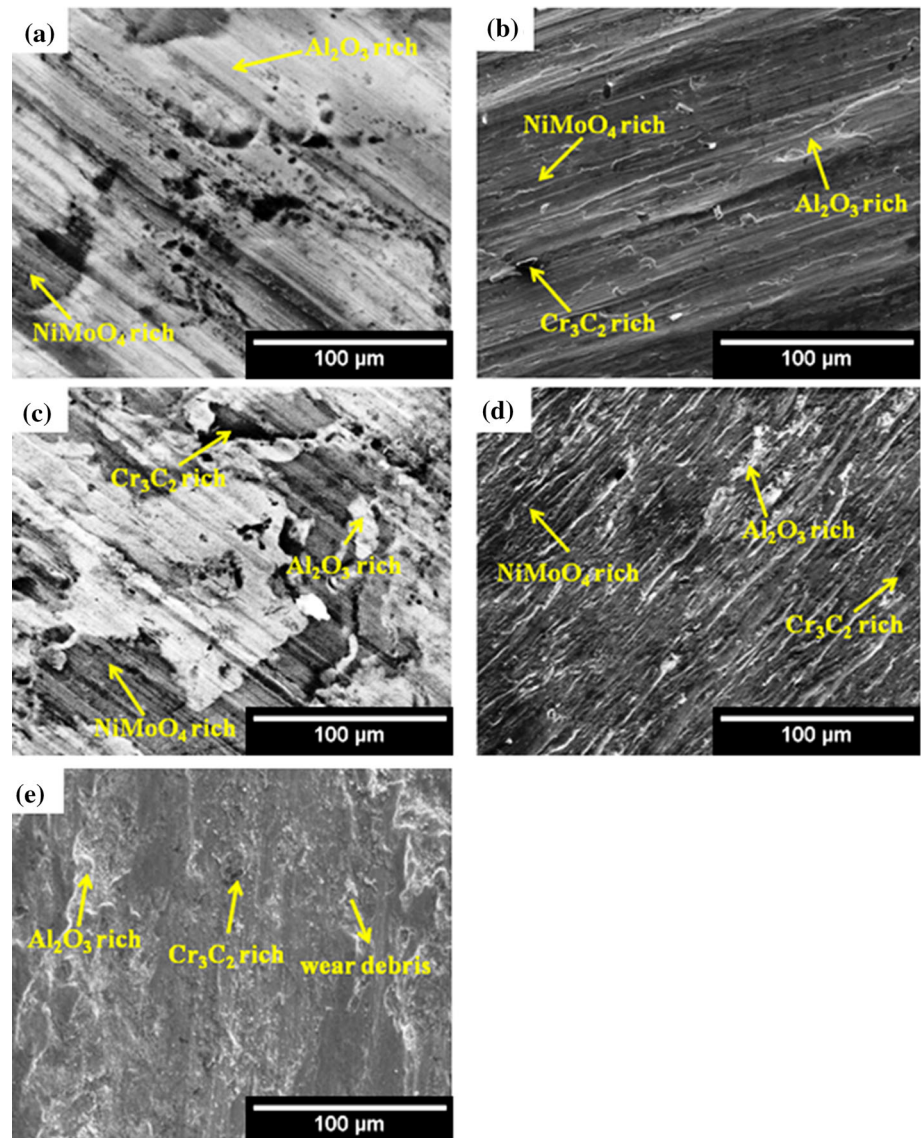
Fig. 12 Optical microscope images of worn surfaces [(a) NiMoAl, (b) NiMoAl-10 wt.% Cr₂AlC, (c) NiMoAl-20 wt.% Cr₂AlC, (d) NiMoAl-50 wt.% Cr₂AlC and (e) Cr₂AlC coating] and their corresponding disk counterparts [(a') NiMoAl, (b') NiMoAl-10 wt.% Cr₂AlC, (c') NiMoAl-20 wt.% Cr₂AlC, (d') NiMoAl-50 wt.% Cr₂AlC and (e') Cr₂AlC coating]



that of NiMoAl-10 wt.% Cr₂AlC coatings. At 50 wt.% Cr₂AlC addition, most of the pores and voids were observed at the interlayer which was indicative of poor interfacial bonding. Based on above observations, the coating life cycle was investigated for NiMoAl and

NiMoAl-20 wt.% Cr₂AlC. The fatigue resistance of the NiMoAl and NiMoAl-20 wt.% Cr₂AlC samples estimated through twist fatigue analysis is found to be 20000 ± 200 and 27000 ± 200 cycles. The obtained result shows that the incorporation of 20 wt.% Cr₂AlC MAX phase in

Fig. 13 BSE micrograph of the worn surface of HVOF-coated (a) NiMoAl, (b) NiMoAl-10 wt.% Cr₂AlC, (c) NiMoAl-20 wt.% Cr₂AlC, (d) NiMoAl-50 wt.% Cr₂AlC and (e) Cr₂AlC samples obtained by FESEM



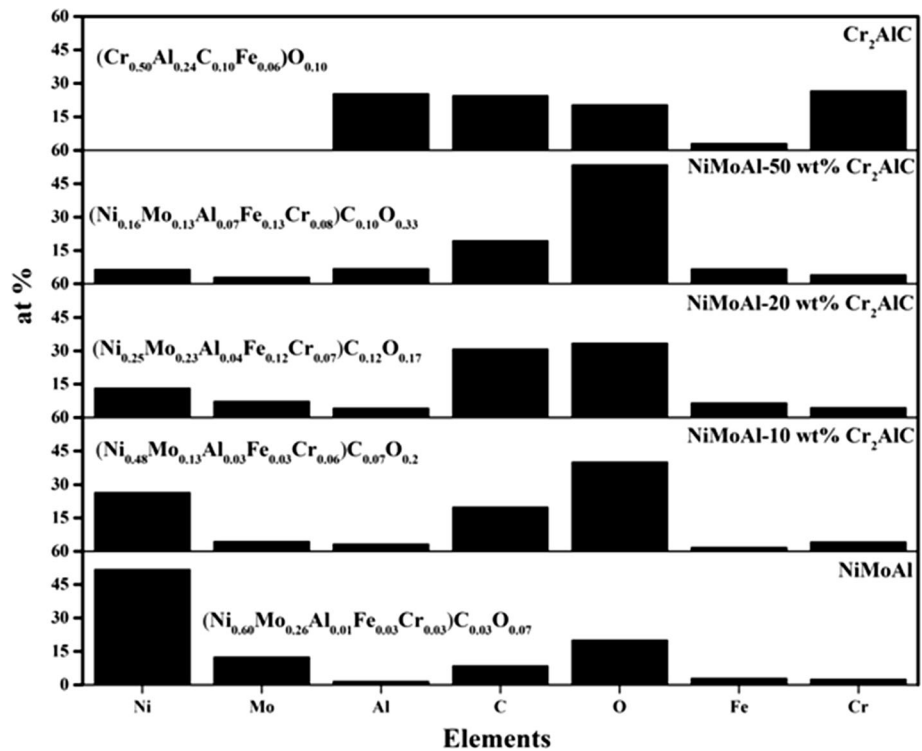
NiMoAl improves its wear and fatigue properties. Figure 16 shows piston rings coated with (a) NiMoAl and (b) NiMoAl-20 wt.% Cr₂AlC, after the twist fatigue test. The NiMoAl-coated piston ring is stable up to 20000 ± 200 cycles; after that, the NiMoAl coating starts to spall. However, the addition of 20 wt.% Cr₂AlC MAX phase in NiMoAl improves the life cycle to 27000 ± 200 cycles. Further increase in cycles resulted in the breaking of the piston ring without spallation of the coating. This

could be due to the improved mechanical properties of 20 wt.% Cr₂AlC-modified NiMoAl coating.

Conclusions

NiMoAl-Cr₂AlC composites were deposited on stainless steel substrate by HVOF spraying. The feedstock powders were prepared by turbo mixing of NiMoAl with different

Fig. 14 Overall elemental analysis of the worn surfaces and its averaged composition



amounts of Cr₂AlC. The average porosity and the wear rate of the NiMoAl, NiMoAl-10 wt.% Cr₂AlC, NiMoAl-20 wt.% Cr₂AlC, NiMoAl-50 wt.% Cr₂AlC and Cr₂AlC coatings are found to be $4.63 \pm 2.50\%$, $3.60 \pm 3.00\%$, $2.13 \pm 1.25\%$, $1.95 \pm 1.55\%$, $7.36 \pm 3.14\%$ and $1.05 \pm 0.47 \times 10^{-5}$, $8.81 \pm 0.32 \times 10^{-6}$, $4.98 \pm 0.18 \times 10^{-6}$, $2.24 \pm 0.29 \times 10^{-5}$, $7.06 \pm 0.53 \times 10^{-7} \text{ mm}^3 \text{ N}^{-1} \text{ m}^{-1}$, respectively. Among all the composite coatings, NiMoAl containing 20 wt.% Cr₂AlC displays the lowest COF and wear rate with optimum porosity (< 2.5%) and excellent

tribo-mechanical properties. The lubricating phase on the worn surface of the composite containing a nearly equal amount of oxygen and carbon along with Cr₂AlC MAX phase result in low COF and wear rate. However, further increase in the amount of reinforcing phase (50 wt.% Cr₂AlC) led to a decrease in the tribo-mechanical properties due to poor interfacial bonding. Incorporation of 20 wt.% Cr₂AlC MAX phase in NiMoAl improves the twist fatigue resistance of the NiMoAl coating to 27000 ± 200 cycles. Based on the results, it can be

Fig. 15 Surface topography images of the worn surfaces and its disk counterparts (a) NiMoAl, (b) NiMoAl-10 wt.% Cr₂AlC, (c) NiMoAl-20 wt.% Cr₂AlC, (d) NiMoAl-50 wt.% Cr₂AlC and (e) Cr₂AlC samples by the three-dimensional surface profiler

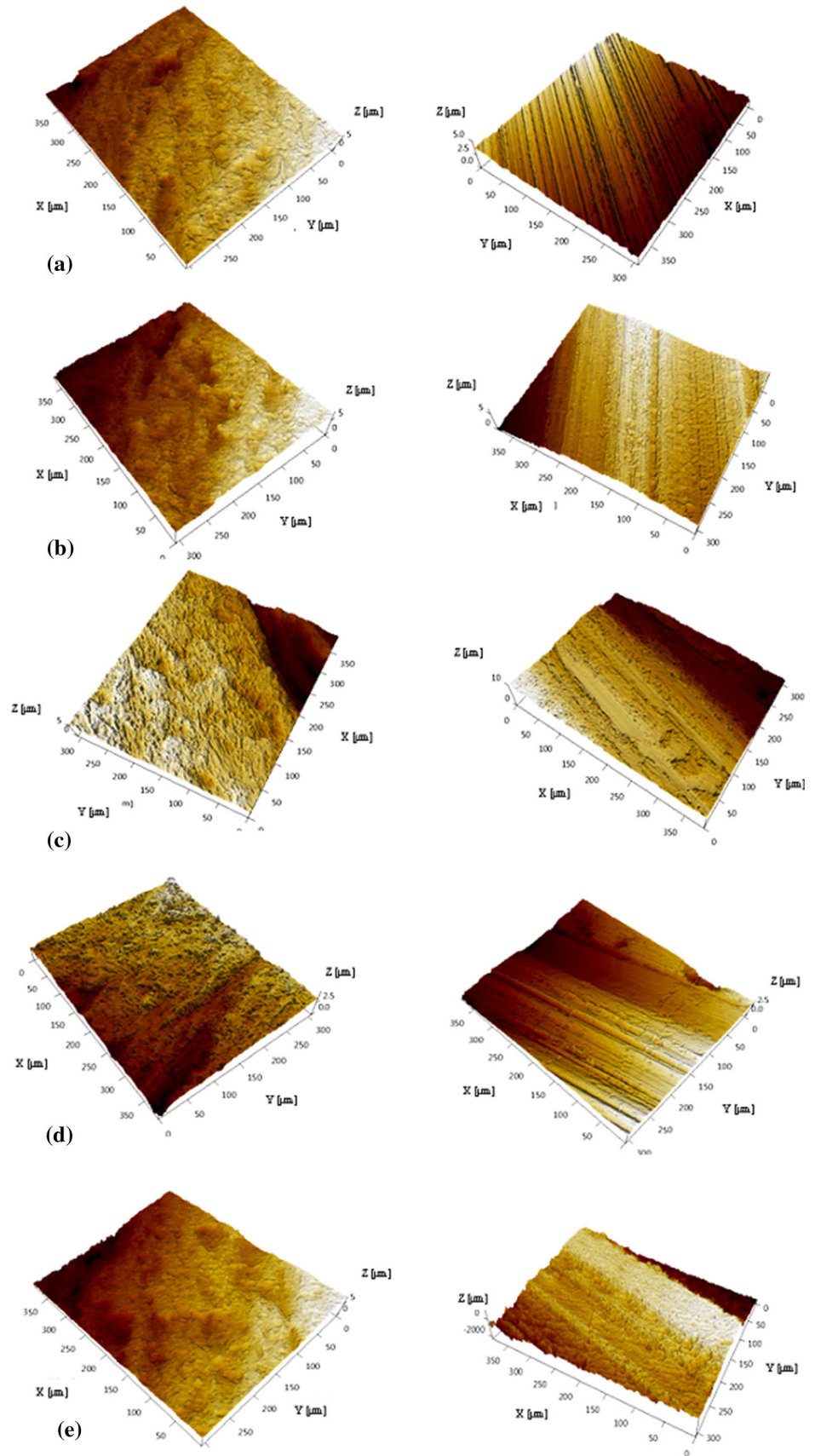
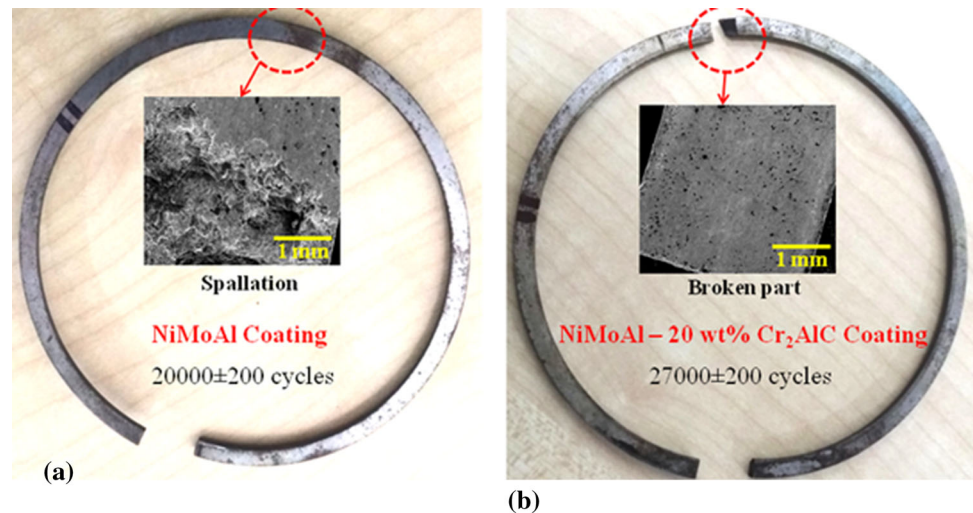


Fig. 16 Twist fatigue life cycle analyzed piston ring coated with (a) NiMoAl and (b) NiMoAl-20 wt.% Cr₂AlC



concluded that the addition of 20 wt.% Cr₂AlC MAX phase enhances the tribo-mechanical properties of the NiMoAl matrix, thereby making it a promising candidate material for tribological application in the automotive sector.

Acknowledgments The authors would like to acknowledge the Director, CSIR-NAL and Head, Surface Engineering Division, CSIR-NAL, for permission to carry out the coating development at CSIR-National Aerospace Laboratories, Bengaluru, Karnataka, India. The authors are thankful to the technical staff of the division for their assistance rendered in the characterization of the coatings. Mr. Deepak Davis acknowledges the ‘Council of Scientific and Industrial Research’, Government of India, New Delhi, India for financial support through CSIR-SRF [CSIR-HRDG reference no. 09/1045(0030)2K19 EMR-I]. The authors also would like to acknowledge the SRM Institute of Science and Technology, Chennai, Tamil Nadu, India for the funding under Selective Excellence Initiative (PNT01) and micro-Raman facility. We acknowledge Nanotechnology Research Centre, SRM Institute of Science and Technology, Chennai, India, for providing FESEM facility.

Conflict of interest The authors declare that they have no known competing financial interests or personal relationships that could have appeared to influence the work reported in this paper.

References

1. C.M. Taylor, Automobile Engine Tribology—Design Considerations for Efficiency and Durability, *Wear*, 1998, **221**(1), p 1–8
2. B.K. Prasad, Sliding Wear Response of a Grey Cast Iron: Effects of Some Experimental Parameters, *Tribol. Int.*, 2011, **44**(5), p 660–667
3. V. Goyal, S.K. Sharma, and B.V. Kumar, Effect of Lubrication on Tribological Behaviour of Martensitic Stainless Steel, *Mater. Today Proc.*, 2015, **2**(4–5), p 1082–1091
4. D.S. Codd, Automotive Mass Reduction with Martensitic Stainless Steel. SAE Technical Paper; 2011
5. D.J. Young, *High Temperature Oxidation and Corrosion of Metals*, Vol 1, Elsevier, Amsterdam, 2008
6. Metals, Special. “High-Performance Alloys for Resistance to Aqueous Corrosion,” *SM Aqueous Corrosion Book*, 2000, p. 28
7. J.R. Davis, Ed., *Nickel, Cobalt, and Their Alloys*, ASM international, 2000
8. P. Andersson, J. Tamminen, and C.E. Sandström, *Piston Ring Tribology: A Literature Survey*, VTT, Espoo, 2002
9. M.L. Parucker, A.N. Klein, C. Binder, W. Ristow Junior, and R. Binder, Development of Self-Lubricating Composite Materials of Nickel with Molybdenum Disulfide, Graphite and Hexagonal Boron Nitride Processed by Powder Metallurgy: Preliminary Study, *Mater. Res.*, 2014, **17**, p 180–185
10. H.E. Sliney, Solid Lubricant Materials for High Temperatures—A Review, *Tribol. Int.*, 1982, **15**(5), p 303–315
11. S. Gupta, D. Filimonov, T. Palanisamy, T. El-Raghy, and M.W. Barsoum, Ta₂AlC and Cr₂AlC Ag-Based Composites—New Solid Lubricant Materials for Use Over a Wide Temperature Range Against Ni-Based Superalloys and Alumina, *Wear*, 2007, **262**(11–12), p 1479–1489
12. M.W. Barsoum, A New Class of Solids: Thermodynamically Stable Nanolaminates, *Prog. Solid State Chem.*, 2000, **28**, p 201
13. J.D. Hettinger, S.E. Lofland, P. Finkel, T. Meehan, J. Palma, K. Harrell, S. Gupta, A. Ganguly, T. El-Raghy, and M.W. Barsoum, Electrical Transport, Thermal Transport, and Elastic Properties of M₂AlC (M = Ti, Cr, Nb, and V), *Phys. Rev. B*, 2005, **72**(11), p 115120
14. F. Cervera, Ed., *ASM Ready Reference: Thermal Properties of Metals*, ASM International, Cleveland, 2002
15. D. Davis, M. Srivastava, M. Malathi, B.B. Panigrahi, and S. Singh, Effect of Cr₂AlC Max Phase Addition on Strengthening of Ni-Mo-Al Alloy Coating on Piston Ring: Tribological and Twist-Fatigue Life Assessment, *Appl. Surf. Sci.*, 2018, **15**(449), p 295–303
16. T.S. Sidhu, S. Prakash, and R.D. Agrawal, Studies on the Properties of High-Velocity Oxy-Fuel Thermal Spray Coatings for Higher Temperature Applications, *Mater. Sci.*, 2005, **41**(6), p 805–823
17. V. Vishnyakov, O. Crisan, P. Dobrosz, and J.S. Colligon, Ion Sputter-Deposition and In-Air Crystallisation of Cr₂AlC Films, *Vacuum*, 2014, **1**(100), p 61–65
18. H.P. Komsa and A.V. Krashennnikov, Effects of Confinement and Environment on the Electronic Structure and Exciton Binding Energy of MoS₂ from First Principles, *Phys. Rev. B*, 2012, **86**(24), p 241201

19. R. Saggari, H. Porwal, P. Tatarko, I. Dlouhý, and M.J. Reece, Boron Nitride Nanosheets Reinforced Glass Matrix Composites, *Adv. Appl. Ceram.*, 2015, **114**(sup1), p S26-S33
20. R.W. Bruce, *Handbook of Lubrication and Tribology, Volume II: Theory and Design*, CRC Press, Boca Raton, 2012
21. R.P. Chakradhar, G. Prasad, K. Venkateswarlu, and M. Srivastava, An Investigation on the Wear and Corrosion Behavior of HVOF-Sprayed WC-12Co-Al₂O₃ Cermet Coating, *J. Mater. Eng. Perform.*, 2018, **27**(3), p 1241-1248
22. Ch Verdon, A. Karimi, and J.-L. Martin, A Study of High Velocity Oxy-Fuel Thermally Sprayed Tungsten Carbide Based Coatings. Part I: Microstructures, *Mater. Sci. Eng. A*, 1998, **246**(1–2), p 11-24
23. J.R. Davis, Ed., *Handbook of Thermal Spray Technology*, ASM International, Cleveland, 2004
24. M.S. Mahdipoor, F. Tarasi, C. Moreau, A. Dolatabadi, and M. Medraj, HVOF Sprayed Coatings of Nano-Agglomerated Tungsten-Carbide/Cobalt Powders for Water Droplet Erosion Application, *Wear*, 2015, **1**(330), p 338-347
25. Š. Houdková, Z. Pala, E. Smazalová, M. Vostřák, and Z. Česánek, Microstructure and Sliding Wear Properties of HVOF Sprayed, Laser Remelted and Laser Clad Stellite 6 Coatings, *Surf. Coat. Technol.*, 2017, **25**(318), p 129-141
26. P. Mi, T. Wang, and F. Ye, Influences of the Compositions and Mechanical Properties of HVOF Sprayed Bimodal WC-Co Coating on Its High Temperature Wear Performance, *Int. J. Refract Metal Hard Mater.*, 2017, **1**(69), p 158-163
27. Y. Rajkumar, B.M. Rahul, P. Ananth Akash, and B.B. Panigrahi, Nonisothermal Sintering of Cr₂AlC Powder, *Int. J. Appl. Ceram. Technol.*, 2017, **14**(1), p 63-67
28. A. Ganvir, N. Curry, S. Björklund, N. Markocsan, and P. Nylén, Characterization of Microstructure and Thermal Properties of YSZ Coatings Obtained by Axial Suspension Plasma Spraying (ASPS), *J. Therm. Spray Technol.*, 2015, **24**(7), p 1195-1204
29. Y. Gao, J. Xiong, D. Gong, J. Li, and M. Ding, Improvement of Solar Absorbing Property of Ni-Mo Based Thermal Spray Coatings by Laser Surface Treatment, *Vacuum*, 2015, **1**(121), p 64-69
30. M. Farber and R.D. Srivastava. The Dissociation Energy of NiO and Vaporization and Sublimation Enthalpies of Ni, *Analytical Calorimetry*, R.S. Porter and J.F. Johnson, Ed., Springer, Boston, 1974, pp. 731–741
31. A.R.C. Nascimento, F.B. Ettouil, C. Moreau, S. Savoie, and R. Schulz, Production of Babbitt Coatings by High Velocity Oxygen Fuel (HVOF) Spraying, *J. Therm. Spray Technol.*, 2017, **26**(7), p 1732-1740
32. L.L. Silveira, G.B. Sucharski, A.G.M. Pukasiewicz, and R.S.C. Paredes, Influence of Particle Size Distribution on the Morphology and Cavitation Resistance of High-Velocity Oxygen Fuel Coatings, *J. Therm. Spray Technol.*, 2018, **27**(4), p 695-709
33. C. Yang, C. Maoyou, W. Lijun, S. Zhixia, W. Xingming, and Z. Bitian. Microstructure and Performance of Cr₂AlC Coatings Deposited by HVOF Spraying. *Chinese Journal of Rare Metals*. 2012, **4**
34. S. Saber-Samandari, K. Alamara, S. Saber-Samandari, and K.A. Gross, Micro-Raman Spectroscopy Shows How the Coating Process Affects the Characteristics of Hydroxylapatite, *Acta Biomater.*, 2013, **9**(12), p 9538-9546
35. J. Chen, X. Zhao, H. Zhou, J. Chen, Y. An, and F. Yan, Microstructure and Tribological Property of HVOF-Sprayed Adaptive NiMoAl-Cr₃C₂-Ag composite coating from 20 C to 800 C, *Surf. Coat. Technol.*, 2014, **15**(258), p 1183-1190
36. J. Chen, X. Zhao, H. Zhou, J. Chen, Y. An, and F. Yan, HVOF-Sprayed Adaptive Low Friction NiMoAl-Ag Coating for Tribological Application from 20 to 800 C, *Tribol. Lett.*, 2014, **56**(1), p 55-66
37. M.S. Ali, A.H.M. Ariff, C.N.A. Jaafar, S.M. Tahir, N. Mazlan, K.A. Maori, and H. Naser, Factors Affecting the Porosity and Mechanical Properties of Porous Ceramic Composite Materials, *Reference Module in Materials Science and Materials Engineering*, 2017. <https://doi.org/10.1016/b978-0-12-803581-8.10131-6>
38. D.B. Lee and Thuan Dinh Nguyen, Cyclic Oxidation of Cr₂AlC Between 1000 and 1300 C in Air, *J. Alloys Compd.*, 2008, **464**(1–2), p 434-439
39. G. Frommeyer, R. Rablbauer, and H.J. Schäfer, Elastic Properties of B2-Ordered NiAl and NiAl-X (Cr, Mo, W) Alloys, *Intermetallics*, 2010, **18**(3), p 299-305
40. W.B. Tian, P.L. Wang, G.J. Zhang, Y.M. Kan, and Y.X. Li, Mechanical Properties of Cr₂AlC Ceramics, *J. Am. Ceram. Soc.*, 2007, **90**(5), p 1663-1666
41. S.M. Hashemi, N. Parvin, and Z. Valefi, Effect of Microstructure and Mechanical Properties on Wear Behavior of Plasma-Sprayed Cr₂O₃-YSZ-SiC Coatings, *Ceram. Int.*, 2019, **45**(5), p 5284-5296
42. A. Souchet, J. Fontaine, J.L. Loubet, Z. Hassan, M. Belin, and M.W. Barsoum, The Role of Tribofilm Evolution on Tribological Behaviour of Ti₃SiC₂ Ceramic. in *Proceeding of World Tribology Congress III 2005 Jan 1*.
43. S. Gupta and M.W. Barsoum, On the Tribology of the MAX Phases and Their Composites During Dry Sliding: A Review, *Wear*, 2011, **271**(9–10), p 1878-1894
44. X.S. Wang, Z.L. Lu, G.T. Lin, L. Jia, and J.X. Chen, Effect of Cr₂AlC Content on the Properties of a Cu-Cr₂AlC Composite, *Results Phys.*, 2016, **1**(6), p 789-795
45. G.V. Kumar, C.S. Rao, and N. Selvaraj, Mechanical and Tribological Behavior of Particulate Reinforced Aluminum Metal Matrix Composites—A Review, *J. Miner. Mater. Charact. Eng.*, 2011, **10**(01), p 59
46. W. Gu, H.F. Wu, S.L. Kampe, and G.-Q. Lu, Volume Fraction Effects on Interfacial Adhesion Strength of Glass-Fiber-Reinforced Polymer Composites, *Mater. Sci. Eng. A*, 2000, **277**(1–2), p 237-243
47. R. Mitra and Y.R. Mahajan, Interfaces in Discontinuously Reinforced Metal Matrix Composites: An Overview, *Bull. Mater. Sci.*, 1995, **18**(4), p 405-434
48. A. Kulkarni, J. Gutleber, S. Sampath, A. Goland, W.B. Lindquist, H. Herman, A.J. Allen, and B. Dowd, Studies of the Microstructure and Properties of Dense Ceramic Coatings Produced by High-Velocity Oxygen-Fuel Combustion Spraying, *Mater. Sci. Eng. A*, 2004, **369**(1–2), p 124-137
49. J. Jie, L. Huan, and L. Xiaohan, Friction and Wear Behavior of Micro Arc Oxidation Coatings on Magnesium Alloy at High Temperature, *Rare Met. Mater. Eng.*, 2017, **46**(5), p 1202-1206
50. A. Ghosh and F. Sadeghi, A Novel Approach to Model Effects of Surface Roughness Parameters on Wear, *Wear*, 2015, **15**(338), p 73-94
51. H. Chen, Y. Du, D. Wang, C. Zhang, G. Yang, B. Liu, Y. Gao, and S. Shi, TiC/Ti₃AlC₂-Co Plasma-Sprayed Coatings with Excellent High-Temperature Tribological Properties, *Ceram. Int.*, 2018, **44**(18), p 22520-22528
52. L. Gudmand-Høyer, A. Bach, G.T. Nielsen, and P. Morgen, Tribological Properties of Automotive Disc Brakes with Solid Lubricants, *Wear*, 1999, **232**(2), p 168-175
53. E. Badisch, C. Mitterer, P.H. Mayrhofer, G. Mori, R.J. Bakker, J. Brenner, and H. Störi, Characterization of Tribo-Layers on Self-Lubricating Plasma-Assisted Chemical-Vapor-Deposited TiN Coatings, *Thin Solid Films*, 2004, **460**(1–2), p 125-132
54. A.S. Rathaur, J.K. Katiyar, and V.K. Patel, Thermo-Mechanical and Tribological Properties of SU-8/h-BN Composite with SN150/perfluoropolyether Filler, *Friction*, 2020, **8**(1), p 151-163
55. A. Shankara, P.L. Menezes, K.R. Simha, and S.V. Kailas, Study of Solid Lubrication with MoS₂ Coating in the Presence of

- Additives Using Reciprocating Ball-on-Flat Scratch Tester, *Sadhana*, 2008, **33**(3), p 207-220
56. M.R. Vazirisereshk, A. Martini, D.A. Strubbe, and M.Z. Baykara, Solid Lubrication with MoS₂: A Review, *Lubricants*, 2019, **7**(7), p 57
57. T.W. Scharf and S.V. Prasad, Solid Lubricants: A Review, *J. Mater. Sci.*, 2013, **48**(2), p 511-531

Publisher's Note Springer Nature remains neutral with regard to jurisdictional claims in published maps and institutional affiliations.